ACS Energy LETTERS

http://pubs.acs.org/journal/aelccp

LETTER

Fluorene-Terminated π-Conjugated Spiro-Type Hole Transport Materials for Perovskite Solar Cells

Mengde Zhai,[▽] Kaihuai Du,[▽] Chengyang Liu, Cheng Chen, Guixiang Li,* Haoxin Wang, Ziyang Xia, Jinman Yang, Hui Xu, Aili Wang,* Toshinori Matsushima, Zhanglin Guo, Meng Li, Antonio Abate, Paul J. Dyson, Mohammad Khaja Nazeeruddin, and Ming Cheng*

Cite This: *ACS Energy Lett.* 2025, 10, 915−924

Read Online

ACCESS | Metrics & More | Article Recommendations | Supporting Information

ABSTRACT: **Spiro-OMeTAD is a widely used hole transport material (HTM) in perovskite solar cells (PSCs), but its inherent low hole mobility and poor thermal stability affect the overall performance of PSCs. To overcome these limitations, we develop a series of fluorene-terminated Spiro-type HTMs, engineered by modulating the fluorene substitution site and π-conjugated intensity. Among these, the *p*-BM material exhibits high energetic ordering in film, appropriate energy levels, and efficient carrier extraction, enabling PSCs to achieve power conversion efficiencies (PCEs) of 25.5% and 24.03% for aperture areas of 0.0625 and 1 cm^2, respectively. Additionally, a perovskite solar mini-module (size 16 cm^2) based on *p*-BM HTM achieved a PCE of 22.4%. More importantly, *p*-BM exhibits a high glass transition temperature and enhanced film hydrophobicity, significantly improving the stability of devices in relation to heat and humidity. Our findings provide a promising alternative HTM for developing efficient and stable perovskite photovoltaic devices.**

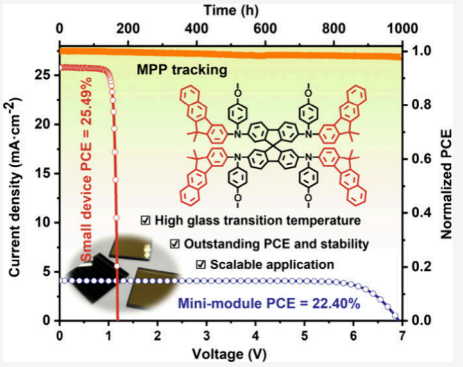

Developing practical renewable energy devices is crucial for driving the global green energy transition. Halide perovskite solar cells (PSCs) have emerged as a leading candidate for next-generation photovoltaic technology due to their low cost and ease of fabrication.[1,2] Following over a decade of development, single-junction PSCs' power conversion efficiency (PCE) now exceeds 26%, competitive with state-of-the-art silicon solar cells.[3−6] Despite the huge improvement in PCEs, long-term stability issues continue to limit the commercialization of PSCs.[7] Typically, the most advanced n-i-p PSCs present a sandwich structure, composed of an n-type electron-selective layer at the bottom, a perovskite absorber in the middle, and a p-type hole transport material (HTM) at the top.[8,9] The HTM is essential in extracting photogenerated holes, blocking reverse electron injection, and inhibiting charge recombination.[10−12] Notably, for n-i-p PSCs, HTMs comprise mostly small organic molecules or polymers whose intrinsic properties significantly affect the hygrothermal stability of the devices.

The small organic molecule, 2,2′,7,7′-tetrakis(*N*,*N*-di-*p*-methoxyphenylamine)-9,9′-spirobifluorene (Spiro-OMeTAD), constructed from a spirobifluorene (Spiro) core and four bis(4-methoxyphenyl)amine donor units, is the most extensively used HTM in PSCs.[13,14] This is due to the well-matched energy levels with the perovskite absorber and the excellent solubility and hence processability.[15,16] However, Spiro-OMeTAD's inherent low conductivity and hole mobility make it difficult to achieve effective hole extraction and transport in the PSC devices.[17−19] Moreover, the Spiro-OMeTAD film is not resistant to high humidity and temperature conditions, resulting in poor PSC stability.[19,20] Although many rigid structured HTMs have been developed to enhance charge mobility and film stability, most of the proposed molecules have yet to achieve satisfactory PCEs.[21−26] Recently, most efforts to improve the PCE and stability of PSCs via modification of the HTM have focused on structural modification of Spiro-OMeTAD. For example, Jeong et al. reported enhanced HTM intrinsic properties by replacing the symmetric peripheral group diphenylamines with asymmetric phenylnaphthylamine edges, improving the device's thermal

Received: November 20, 2024
Revised: December 29, 2024
Accepted: January 17, 2025
Published: January 23, 2025

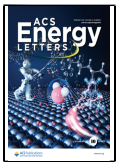

stability (>78.5% PCE retention after 400 h at 60 °C).[27] Another approach is to increase the π conjugation, which could improve the hole mobility. Spiro-type HTMs introducing conjugated units, such as polycyclic fluorene, carbazole, dibenzofuran, and biphenyl in the periphery, have been reported.[4,28−31] Jeon et al. introduced 9,9-dimethylfluorene as the π-conjugation periphery and synthesized an HTM termed DM, which significantly enhanced the efficiency of PSCs.[31] Although considerable benefits were obtained with this strategy, the influence of π-conjugated units on the material properties and performance aspects lacks detailed studies. Therefore, systematically investigating the effect of π-conjugation strategies on the performance of Spiro-type HTMs will further advance the progress of the PSCs.

In this work, we designed and synthesized three Spiro-type HTMs, DM, *p*-DM, and *p*-BM, by incorporating different fluorene structural units with various substitution sites and π-conjugated intensity. We investigated the influence of the conjugation position (C_4 position for DM; C_3 position for *p*-DM) and the conjugation intensity (for *p*-BM) on their physicochemical and optoelectronic properties. We found that repositioning the fluorene connection from the C_4 to the C_3 site significantly enhances the energetic ordering of HTM films. Moreover, extending the conjugated strand in *p*-BM increases its glass transition temperature (T_g) to 211.8 °C, significantly enhancing the thermal stability of the films and the resulting PSC devices. The optimized fluorene-terminated π-conjugation system enhances charge transport and energy level alignment. The *p*-BM HTM exhibits the highest conductivity and deeper Fermi levels (E_F) promoting charge transfer at the perovskite/HTM interface and reducing nonradiative recombination. Consequently, PSCs based on *p*-BM achieved PCEs of 25.49% and 24.03% for 0.0625 and 1.0 cm^2 aperture areas, respectively. Perovskite solar mini-modules with a 16 cm^2 aperture area delivered a PCE of 22.40%. *p*-BM based unencapsulated PSCs demonstrated excellent humidity and thermal and operational stability.

The structures of the conventional HTM Spiro-OMeTAD and fluorene-terminated Spiro-type HTMs are shown in Figure 1. DM, *p*-DM, and *p*-BM were synthesized via a two-step route comprising two $Pd_2(dba)_3$-catalyzed Buchwald−Hartwig coupling steps, in which the first step yielded the peripheral donor substituted with the fluorene unit and the second step coupled the 2,2′,7,7′-tetrabromo-9,9′-spirobifluorene core with the four peripherals; see Scheme S1 in the Supporting Information (SI). The structures of these HTMs were characterized by ^1H and ^{13}C NMR spectroscopy and MALDI-TOF mass spectrometry (Figures S1−S12). Benefiting from the highly twisted skeleton of the Spiro core, all three HTMs possess good solubility in commonly used organic solvents (ethyl acetate, dichloromethane, tetrahydrofuran, and chlorobenzene) of >240 mg/mL (Figure S13), which facilitates thin film deposition.[21,32]

The normalized ultraviolet−visible absorption (UV−vis) spectra of DM, *p*-DM, and *p*-BM in solution and solid state are shown in Figure S14. In dichloromethane solution, DM, *p*-DM, and *p*-BM exhibit maximum absorption peaks at 402, 387, and 373 nm, respectively, with the energy gaps (E_g) determined to be 2.93, 3.00, and 2.97 eV, respectively, based on $E_g = 1240/\lambda_{onset}$. The spectra of all three materials are slightly red-shifted in the film state compared to in solution, which may be attributed to closer molecular packing and enhanced intermolecular interactions.[31,33] The temperature-dependent

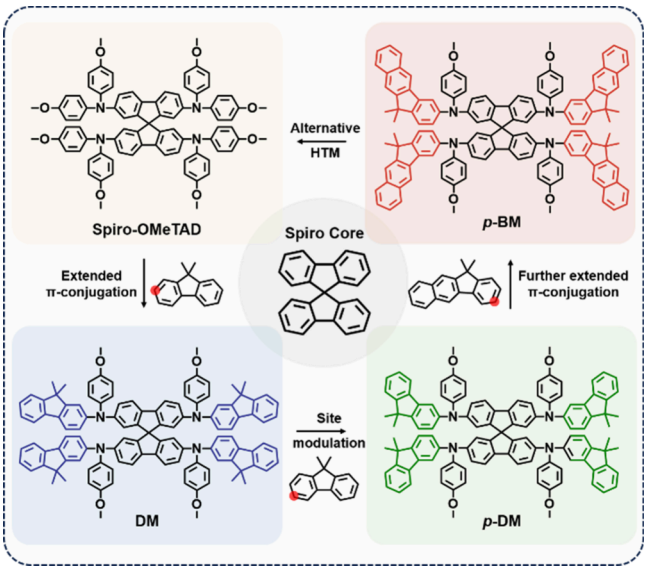

Figure 1. Structures of Spiro-OMeTAD, DM, *p*-DM, and *p*-BM and a summary of the design strategy.

UV−vis spectra in Figure 2a−c show that these materials all possess temperature-dependent aggregation properties. Notably, *p*-DM and *p*-BM display one absorption peak at 100 °C and two separate absorption peaks at 0 °C, and the outer shoulder peak increases significantly with decreasing temperature. This suggests that the temperature-dependence aggregation properties of *p*-DM and *p*-BM are slightly stronger than DM, attributed to the enhanced π-conjugation system of the fluorene terminal unit.[30,34,35] Subsequently, considering the temperature impact on charge hopping in semiconductor materials, we further constructed hole only devices to evaluate the energetic ordering of HTM films.[36] Generally, organic semiconductors with weak intermolecular interactions will lead to disordered molecular stacking and exhibit a strong temperature dependence owing to the high activation energy.[37] As shown in Figure 2d−f and Figure S15, the carrier mobility of *p*-BM films is much less responsive to temperature, with a disorder parameter (σ) of only 38 meV, which is much lower than that of 64 and 98 meV for *p*-DM and DM. This indicates that the *p*-BM molecules generate a high energy ordering in the films, which would be favorable for carrier extraction and transport.[38,39] Cyclic voltammetry (CV) measurements (Figure 2g) reveal that the highest occupied molecular orbital (HOMO) energy levels for DM, *p*-DM, and *p*-BM are −5.12, −5.12, and −5.13 eV, respectively. Among these HTMs, *p*-BM exhibits deeper HOMO levels, probably due to the weaker electron-donating capacity of the extended fluorene units. Density functional theory (DFT) simulations (Figure S16) show that the electron density of the lowest unoccupied molecular orbital (LUMO) of *p*-DM and *p*-BM transfers broadly toward the fluorene end-groups due to π-conjugated extensions of the peripheral unit, which could promote the intermolecular charge transfer and thus enhance the device carrier transport.[30,31] Note, the gas state during the simulation and the liquid state during the CV measurement might be responsible for the inconsistent energy levels.[40,41] In addition, the electrostatic potential (ESP) of *p*-BM shows that it has a weak charge-polarized structure, indicating it should have good electrochemical stability (Figure S17).[28,42,43]

https://doi.org/10.1021/acsenergylett.4c03233
ACS Energy Lett. 2025, 10, 915−924

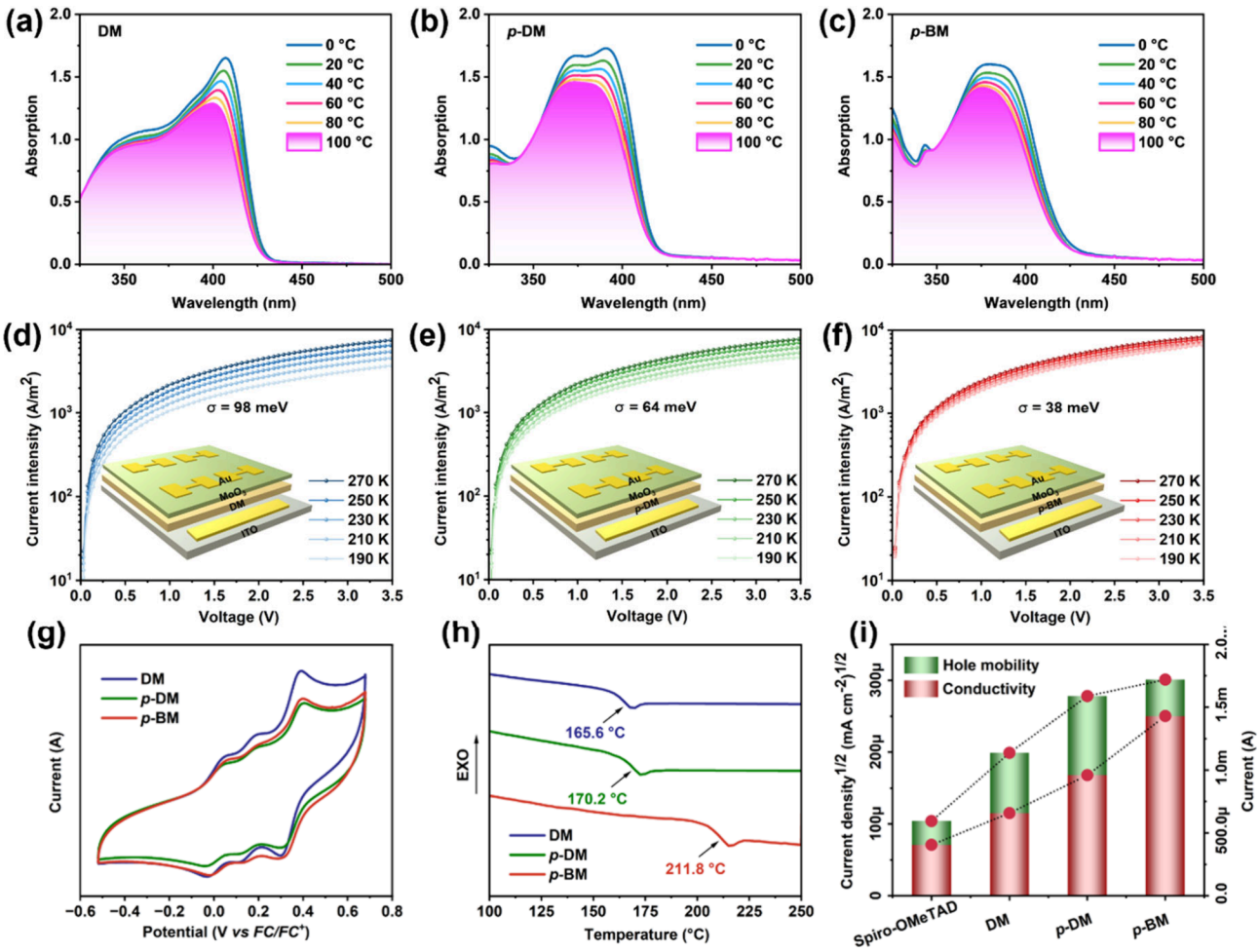

Figure 2. UV−vis absorption spectra of (a) DM, (b) *p*-DM, and (c) *p*-BM in chlorobenzene as a function of the temperature. Temperature-dependent dark-state *J*−*V* curves of (d) DM, (e) *p*-DM, and (f) *p*-DM films. Inset: schematic illustration of the device structure. (g) CV curves of DM, *p*-DM, and *p*-BM. (h) DSC curves of DM, *p*-DM, and *p*-BM. (i) Statistical diagrams of hole mobility and conductivity values for doped Spiro-OMeTAD, DM, *p*-DM, and *p*-BM films.

Modulation of the fluorene terminated π-conjugated system also impacts the thermal stability of the HTMs. Thermogravimetric analysis (TGA) reveals that the decomposition temperatures (T_d) of HTMs at 5% weight loss all exceed 450 °C (Figure S18), which is much higher than the thermal degradation temperature of perovskite crystals.[44] Differential scanning calorimetry (DSC) data affords a T_g value of 211.8 °C for *p*-BM mainly attributed to the increased conjugation intensity and significantly larger molecular weight, which is much higher than that of *p*-DM (170.2 °C) and DM (165.6 °C) and is almost 100 °C higher than Spiro-OMeTAD (Figure 2h).[45] The T_g for *p*-BM is also one of the highest values among Spiro-type HTMs (Table S7). Thus, the excellent thermal stability of *p*-BM should allow it to function at high operating temperatures (the optical, electrochemical, and thermal properties of these materials are summarized in Table S1).

The film morphology and electronic properties of HTMs deposited on perovskite films were investigated. Scanning electron microscope (SEM) images (Figure S19) show that all three fluorene-terminated HTM films are uniform and dense, whereas the Spiro-OMeTAD film exists with many harmful pinholes. The film surface's root-mean-squared (RMS) roughness was measured using atomic force microscopy (AFM). As shown in Figure S20, the *p*-DM and *p*-BM films exhibit smoother surfaces with RMS of 16.6 and 16.3 nm, respectively, compared to 22.3 and 19.2 nm for the Spiro-OMeTAD and DM films. The dense and homogeneous film morphology facilitates interfacial contact and hole transport. Accordingly, conductive atomic force microscopy (C-AFM) measurements provide an average conductivity (σ_0) of 33.4, 45.1, and 91.6 pA for the DM, *p*-DM, and *p*-BM films, respectively (Figure 3d−f). The σ_0 value was verified by conductivity measurements; see Figure S21 and Table S2. The hole mobility was also evaluated by using the space-charge-limited current (SCLC) method (Figure S22 and Table S3). The results show that the hole mobility of the doped DM, *p*-DM, and *p*-BM films are 1.99×10^{-4}, 2.78×10^{-4}, and 3.01×10^{-4} $cm^2 \cdot V^{-1} \cdot s^{-1}$, respectively, which agrees well with the trend of hole transfer integrals from the simulations of their dimers (Figure S23). The charge transport capacities of these fluorene-terminated HTMs are higher than those of the conventional HTM Spiro-OMeTAD (Figure 2i), which can be attributed to the elevated molecular π-conjugation as well as the enhanced intermolecular interactions.

The energy level structure of the HTMs was explored using ultraviolet photoelectron spectroscopy (UPS); see Figure 3a,b. The secondary electron cutoffs (E_{cutoff}) of the DM, *p*-DM, and *p*-BM films are 17.91, 17.69, and 17.66 eV, respectively, and

https://doi.org/10.1021/acsenergylett.4c03233
ACS Energy Lett. 2025, 10, 915−924

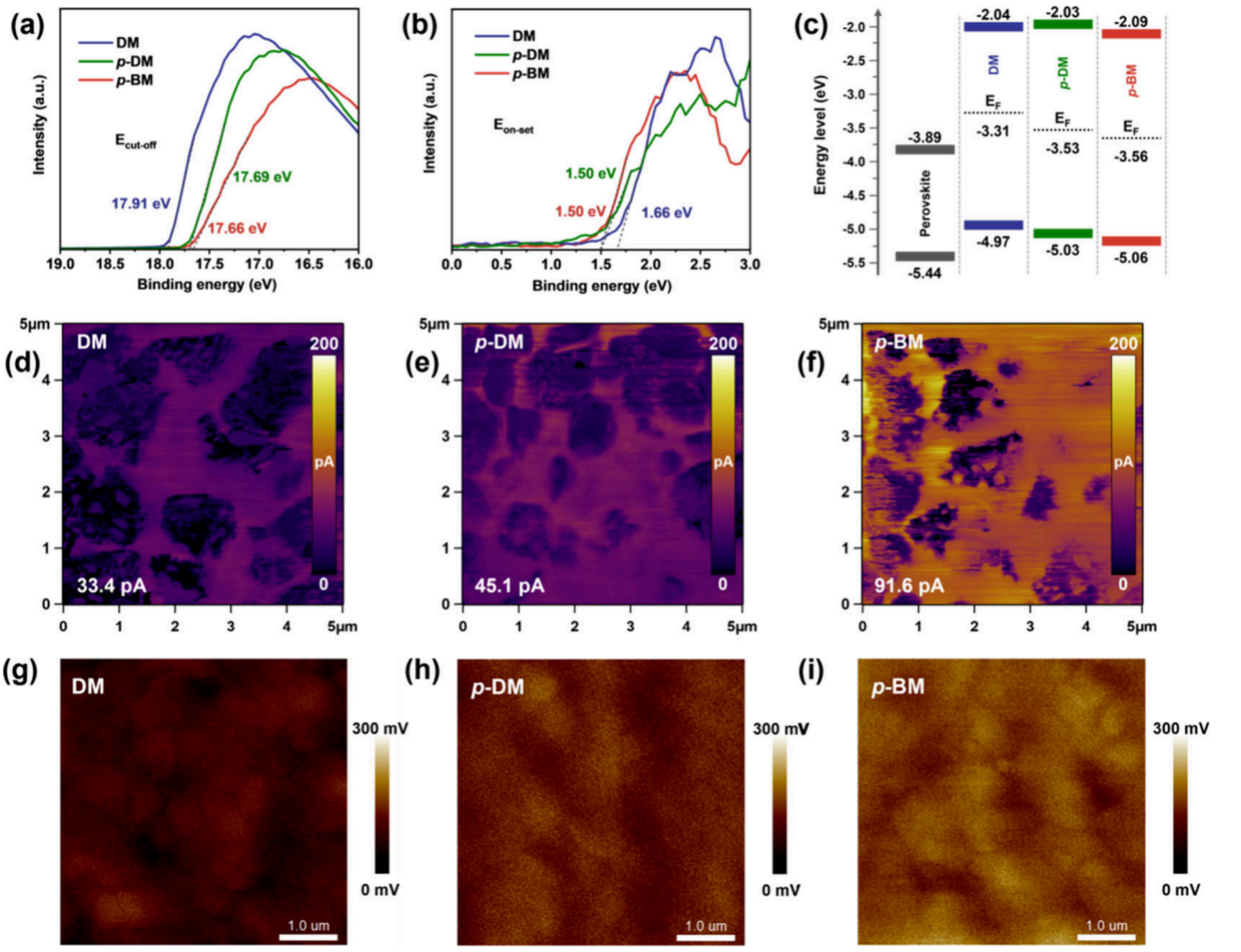

Figure 3. (a) Secondary electron cutoff and (b) valence band of UPS spectra for the DM, *p*-DM, and *p*-BM films. (c) Energy-level diagrams for perovskite, DM, *p*-DM, and *p*-BM films. C-AFM images of (d) DM, (e) *p*-DM, and (f) *p*-BM HTMs coated on perovskite films. KPFM images of (g) DM, (h) *p*-DM, and (i) *p*-BM HTMs coated on perovskite films.

the corresponding E_F were calculated as −3.31, −3.53, and −3.56 eV, respectively. The more negative E_F is beneficial for energy level alignment and promotes hole extraction by HTM from the perovskite,[13,46,47] which was confirmed by Kelvin probe force microscopy (KPFM). As shown in Figure 3g−i, the surface potentials of the HTM films follow a *p*-BM > *p*-DM > DM trend, consistent with the UPS results. Furthermore, combined with the E_F values, the ionization potentials of the DM, *p*-DM, and *p*-BM films were calculated as −4.97, −5.03, and −5.06 eV, respectively. The HOMO levels obtained by photoelectron spectroscopy in air (PESA) also closely match the values measured via the UPS (Figure S24). Figure 3c shows the energy level arrangement of the perovskite and the HTM layers. The *p*-BM has deeper E_F and HOMO energy level, aligning well with the valence band of the perovskite layer, which should help to minimize voltage losses in PSCs.[4,22,48]

To investigate the effect of the HTMs on photovoltaic performance, we fabricated n-i-p PSCs with an architecture comprising the FTO/TiO_2/SnO_2/$(FAPbI_3)_{0.992}(MAPbBr_3)_{0.008}$/HTM/Au electrode. A corresponding cross-sectional SEM image with *p*-BM is shown in Figure 4a, with the thickness of the *p*-BM HTM layer being around 140 nm. A comparison of the best *J*−*V* curves of the PSCs based on doped DM, *p*-DM, and *p*-BM HTMs under AM 1.5G illumination are shown in Figure 4b. The DM based devices have a PCE of 24.11% with an open-circuit voltage (V_{OC}) of 1.158 V, a short-circuit current density (J_{SC}) of 25.28 mA cm^{-2}, and a fill factor (*FF*) of 82.37%. The *p*-DM based PSCs achieve a PCE of 24.86% with a V_{OC} of 1.174 V, a J_{SC} of 25.60 mA cm^{-2}, and an *FF* of 82.69%. With the extended fluorene π-conjugated system in *p*-BM, the resulting PSCs achieved a PCE of 25.49% accompanied by a V_{OC} of 1.184 V, a J_{SC} of 25.77 mA cm^{-2}, and an *FF* of 83.56%. To the best of our knowledge, a PCE of 25.49% is among the highest values for n-i-p PSCs employing Spiro-type HTMs (Table S7). This enhanced device performance was attributed to the *p*-BM well-matched energy levels and excellent charge transport properties. Figure 4c shows the external quantum efficiency (EQE) spectra, with the integrated J_{SC} values estimated as 24.19, 24.49, and 24.77 mA cm^{-2} for the DM, *p*-DM, and *p*-BM based devices, respectively, which agrees well with the J_{SC} values obtained from the *J*−*V* measurements. Furthermore, the device performance of the fluorene-terminated HTMs is higher than that of conventional Spiro-OMeTAD (Figures S25 and S26).

Stabilized photocurrents and PCEs of the PSCs based on three different HTMs were recorded at maximum power points (1.01 V for DM, 1.02 V for *p*-DM, and 1.04 V for *p*-

https://doi.org/10.1021/acsenergylett.4c03233
ACS Energy Lett. 2025, 10, 915−924

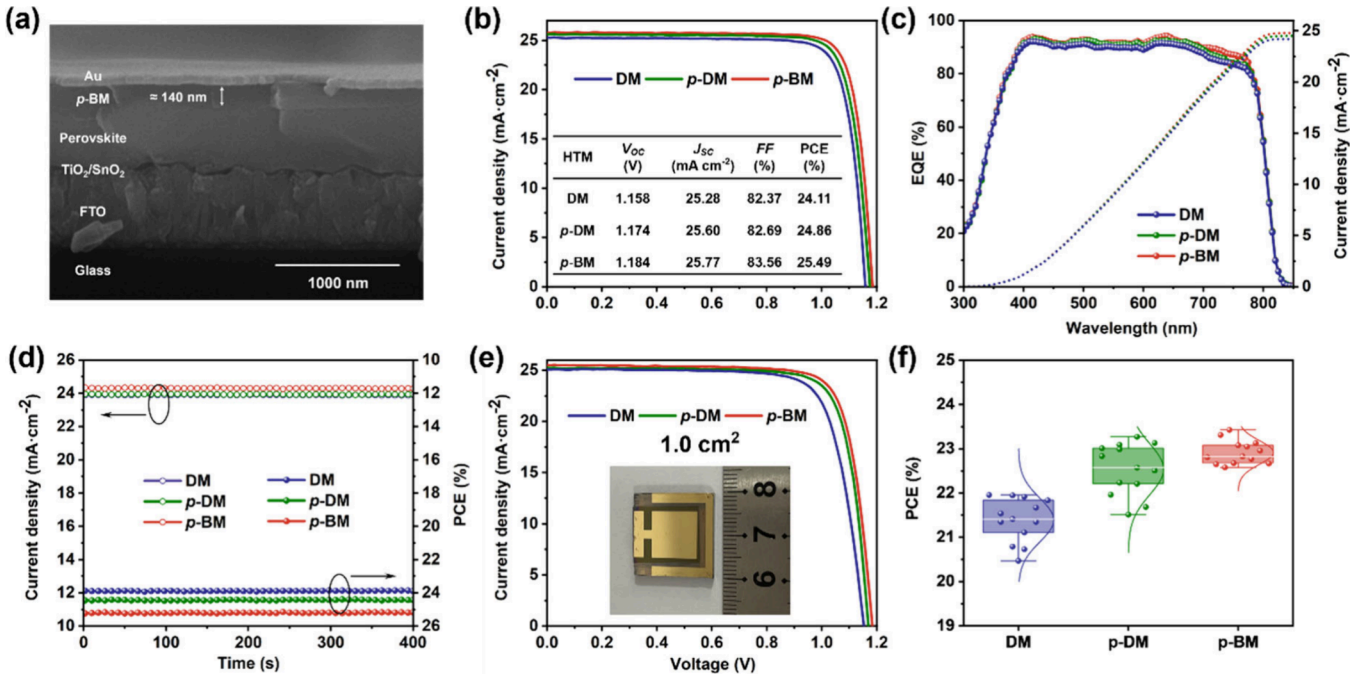

Figure 4. (a) Cross-sectional SEM image of the *p*-BM based PSC. (b) *J*−*V* curves of the PSCs based on DM, *p*-DM, and *p*-BM HTMs under AM 1.5G 100 mW cm^{-2} illumination (active area of 0.0625 cm^2). (c) EQE curves of the PSCs based on DM, *p*-DM, and *p*-BM HTMs. (d) Stabilized PCEs and J_{SC} for PSCs based on DM, *p*-DM, and *p*-BM HTMs. (e) *J*−*V* curves of 1.0-cm^2 PSCs based on DM, *p*-DM, and *p*-BM HTMs. (f) Statistics of PCEs for DM, *p*-DM, and *p*-BM based PSCs with a large area (1.0 cm^2).

BM) (Figure 4d). We obtained the stabilized PCEs of 23.87%, 24.33%, and 25.24% for the DM, *p*-DM, and *p*-BM based devices, respectively. The device's hysteresis index (HI) based on DM, *p*-DM, and *p*-BM are 4.8%, 3.9%, and 3.3%, respectively (Figures S27−S29). Additionally, the PSCs based on different HTMs show excellent reproducibility (Figure S30). To further evaluate the performance of the three HTMs, large-area (1.0 cm^2) PSCs were also fabricated (Figure 4e and Table S4). Champion PCEs of 22.38%, 23.48%, and 24.03% were achieved for the DM, *p*-DM, and *p*-BM based PSCs with an aperture area of 1.0 cm^2, respectively. Figure 4f depicts the statistical distribution of PCEs for the corresponding devices. Notably, the reproducibility of the large-scale PSCs based on *p*-BM is superior to that of DM and *p*-DM.

The excellent photovoltaic performance of the *p*-BM based PSCs may also be attributed to boosted hole extraction, as evidenced from steady-state photoluminescence (PL); see Figure S31. PL mapping was also conducted to investigate the quenching intensity of the HTMs on the perovskite from the perspective of a two-dimensional (2D) surface (Figure 5a−c). The data demonstrate that the perovskite/*p*-BM films exhibit quenching efficiencies higher than those of the perovskite/DM and perovskite/*p*-DM films, along with improved emission uniformity. From time-resolved photoluminescence (TRPL) measurements, the τ_{ave} of the perovskite film is reduced from 184.1 ns for the bare sample to 138.0, 110.9, and 97.9 ns, after coating with DM, *p*-DM, and *p*-BM, respectively (Figure 5g and Table S5). The more efficient hole extraction and interfacial transport of *p*-BM were attributed to the enhanced hole mobility and conductivity resulting from its extended p-conjugated system.[24,49] Femtosecond transient absorption spectroscopy (fs-TAS) measurements were carried out to further elucidate the ultrafast carrier dynamics at the interface of the perovskite/HTM.[50,51] As shown in Figure 5d−f and Figure S32, all samples exhibit a primary photobleaching (PB) peak ($\Delta A < 0$) at the band edge position at around 769 nm, which gradually weakens with time. Moreover, within the same delay time, the varying intensity of the PB peaks for the different films implies there are differences in the carrier separation rates.[52] The decay kinetics of the PB peak was investigated by fitting the exciton lifetimes of the fs-TAS using a biexponential decay function (Figure 5h), and the relevant parameters are summarized in Table S6. The fast lifetime (τ_1) is related to hole extraction from photoexcited perovskite to the valence band of the HTM. Compared with the τ_1 value of 319.2 ps for the perovskite/DM sample, the shorter τ_1 of perovskite/*p*-DM (236.7 ps) and perovskite/*p*-BM (104.5 ps) samples indicates an increased speed of hole injection, which explains the enhancement of V_{OC} in the *p*-DM and *p*-BM based PSCs. The slow decay (τ_2) might be assigned to excited-state decay or carrier recombination in the perovskite films, and τ_2 values for perovskite/DM, perovskite/*p*-DM, and perovskite/*p*-BM are 3414.6, 1485.0, and 1174.6 ps, respectively. The shorter τ_2 value of the perovskite/*p*-BM sample indicates that carrier separation is more effective, with the holes rapidly transferred to the back electrode.[50]

To further elucidate the charge recombination mechanism in the PSCs, the dependence of V_{OC} on the light intensity was studied. As shown in Figure S33, the slopes of the fitting curves are in the following order: DM based device (1.71 kT/q) > *p*-DM based device (1.32 kT/q) > *p*-BM based device (1.21 kT/q). A lower slope value indicates that defect-induced Shockley−Read−Hall recombination is significantly inhibited, i.e., as in the *p*-BM based devices.[53] This observation is also supported by electrochemical impedance spectroscopy (EIS) measurement (Figure S34), where *p*-BM based PSCs exhibit relatively larger charge recombination resistance (R_{rec}). Mott−Schottky plots further reveal that the built-in potential (V_{bi}) of

https://doi.org/10.1021/acsenergylett.4c03233
ACS Energy Lett. 2025, 10, 915−924

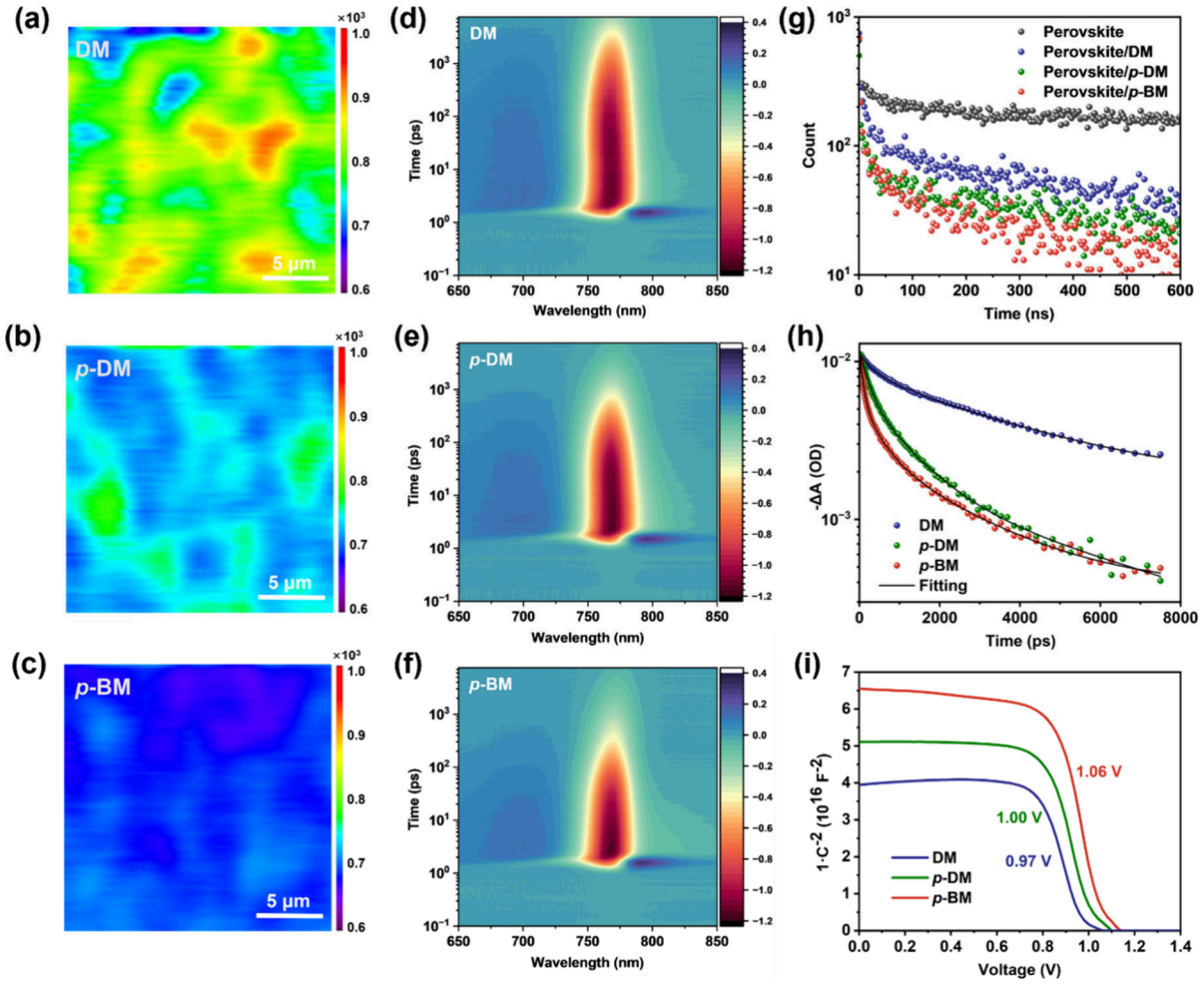

Figure 5. PL mapping of (a) DM, (b) *p*-DM, and (c) *p*-BM coated perovskite films. Pseudocolor fs-TAS plot of (d) glass/perovskite/DM, (e) glass/perovskite/*p*-DM, and (f) glass/perovskite/*p*-BM samples pumped at 2.41 eV. The pump laser is incident from the glass side. (g) TRPL spectra of the perovskite films coated with DM, *p*-DM, and *p*-BM HTMs. (h) Normalized decay kinetic curves of fs-TAS for glass/perovskite/DM, glass/perovskite/*p*-DM, and glass/perovskite/*p*-BM samples at 769 nm. (i) Mott−Schottky plots of PSCs based on DM, *p*-DM, and *p*-BM HTMs.

the *p*-BM based PSCs is estimated to be 1.06 V, higher than that of *p*-DM (1.00 V) and DM (0.97 V) (Figure 5i). The appreciable increase in the V_{bi} of the *p*-BM based PSCs confirms the larger driving force for carrier separation and transfer, resulting in less interfacial charge accumulation.

We performed water contact angle measurements to analyze the hydrophobicity of the HTM films. As shown in Figure 6a, the water contact angles of the DM, *p*-DM, and *p*-BM films are 94.6°, 94.9°, and 105.6°, respectively, compared to the water contact angle of the bare perovskite film of 76.1°. The superior hydrophobic barrier provided by the *p*-BM HTM should prevent the degradation of the perovskite film upon moisture exposure. Subsequently, we evaluated the long-term humidity stability of the PSCs by tracking the PCE evolution of the unencapsulated devices under ambient conditions with a relative humidity (RH) of 30−40%. After storage for up to 4,000 h, the DM, *p*-DM, and *p*-BM based PSCs maintained 43.5%, 75.0%, and 93.8% of their initial PCEs, respectively (Figure 6b). We also compared the stability of perovskite with *p*-BM and Spiro-OMeTAD coated films under >85% high RH conditions (Figure S35). Obviously, the black phase of perovskite coated with *p*-BM films remained longer, indicating excellent resistance to moisture. The influence of the HTMs on the thermal stability of PSCs at 85 °C was also evaluated in a glovebox filled with N_2. As shown in Figure 6c, the difference in the performance degradation of PSCs based on different HTMs is minor during the initial 240 h period; however, the decay rate varies thereafter. The thermal aging tests demonstrate that the *p*-BM based PSCs are more thermally stable, retaining 80.4% of the initial efficiency after aging at 85 °C for 500 h, attributable to the high T_g of 211.8 °C of *p*-BM, which inhibits the transition of the HTM film from an amorphous state to a crystalline state. Additionally, the unencapsulated *p*-BM based PSCs maintain 97.9% performance after 1,000 h under continuous irradiation (AM1.5G, N_2) at the maximum power point (Figure 6d), highlighting its outstanding operational stability.

To assess the scalability of the novel *p*-BM materials for large-area applications, we fabricated a batch of 4 × 4 cm^2 perovskite solar mini-modules to evaluate the scale-up potential of the *p*-BM HTM, as shown in Figure 6e. The modules achieved a champion PCE of 22.40%, with a V_{OC} of 6.935 V, a J_{SC} of 4.11 mA cm^{-2}, and an *FF* of 78.71%, representing a highly competitive efficiency value (Figure 6f).

In summary, we developed a class of fluorene-terminated Spiro-type HTMs in which the site and size of the *π*-

https://doi.org/10.1021/acsenergylett.4c03233
ACS Energy Lett. 2025, 10, 915−924

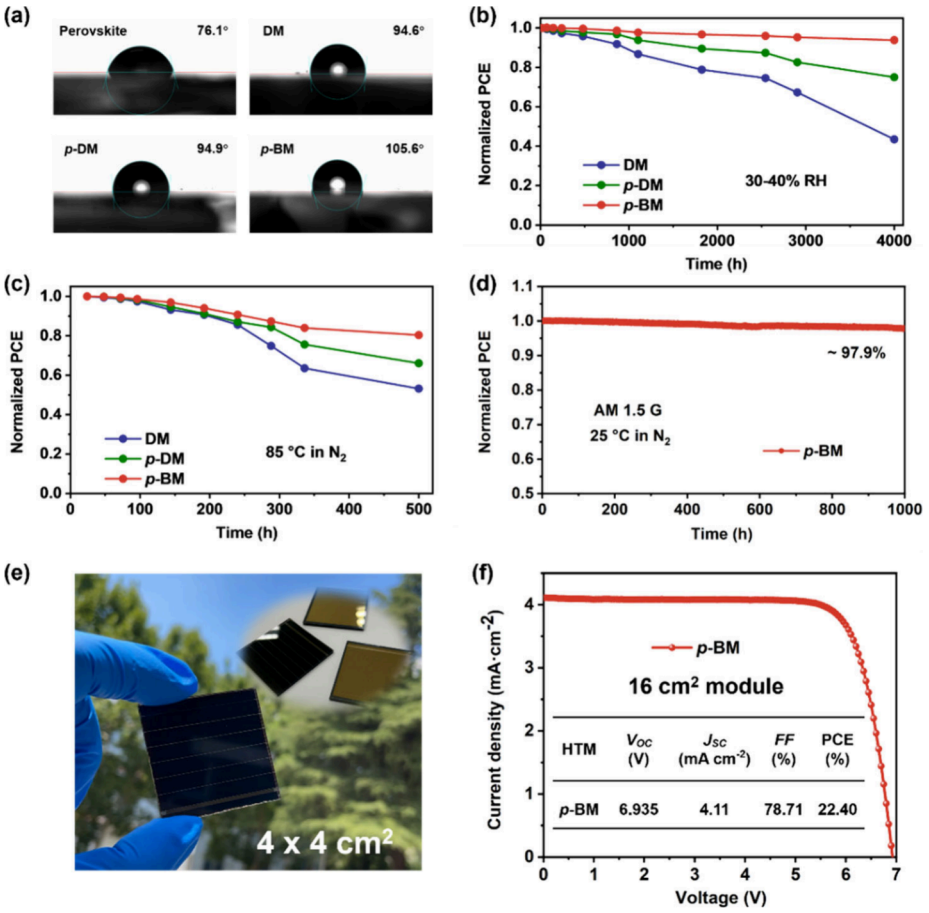

Figure 6. (a) Water contact angles for bare perovskite and the DM, *p*-DM, and *p*-BM HTM-coated films. (b) Long-term stability of the unencapsulated PSCs in air with 30−40% RH. (c) Thermal stability of the unencapsulated PSCs at 85 °C. (d) Operational stability of the unencapsulated *p*-BM based PSCs under AM1.5G solar illumination in a N_2 atmosphere at the maximum power point. (e) Photographs of sealed 4 × 4 cm^2 *p*-BM based solar modules with an active area of 12.1 cm^2 according to the average of six separate cells. (f) The *J*−*V* curve of the solar module based on the *p*-BM HTM.

conjugated system strongly influence their properties, specifically enhancing carrier extraction and shifting the E_F to better match the perovskite valence band. These new HTMs were evaluated in PSCs and mini-modules, with the PSCs based on the *p*-BM HTM affording PCEs of 25.5% and 24.03% for devices with aperture areas of 0.0625 and 1 cm^2, respectively. Unencapsulated devices exhibit excellent stabilities under continuous one sun exposure tracked at MPP, at elevated 85 °C and in ambient air with a 30−40% RH. Moreover, we fabricated a mini-module with a size of 16 cm^2 using *p*-BM as the HTM, achieving a champion PCE of 22.4%. The approach highlights that Spiro-type HTMs may be enhanced using molecular design strategies. Given the excellent properties and scalability of the *p*-BM HTM, this specific molecule is a promising candidate for applications in PSCs and other optoelectronic devices.

■ ASSOCIATED CONTENT

Supporting Information

The Supporting Information is available free of charge at https://pubs.acs.org/doi/10.1021/acsenergylett.4c03233.

Detailed description of the experimental methods, including reagent sources, material synthesis, characterization analysis, device fabrication, and additional data (PDF)

■ AUTHOR INFORMATION

Corresponding Authors

Guixiang Li − *Institute of Chemical Sciences and Engineering, École Polytechnique Fédérale de Lausanne (EPFL), CH-1015 Lausanne, Switzerland; Helmholtz-Zentrum Berlin für Materialien und Energie GmbH, Berlin 14109, Germany;* orcid.org/0000-0002-8730-0713; Email: guixiang.li.gl@gmail.com

Aili Wang − *Institute of Technology for Carbon Neutralization, Yangzhou University, Yangzhou 225127 Jiangsu, China*; Email: wangal@yzu.edu.cn

Ming Cheng − *Institute for Energy Research, School of Energy and Power Engineering, School of Environment and Safety Engineering, Jiangsu University, Zhenjiang 212013, China;* orcid.org/0000-0003-0793-0326; Email: mingcheng@ujs.edu.cn

Authors

Mengde Zhai − *Institute for Energy Research, School of Energy and Power Engineering, School of Environment and Safety Engineering, Jiangsu University, Zhenjiang 212013, China; International Institute for Carbon-Neutral Energy Research (WPI-I2CNER), Kyushu University, Fukuoka 819-0395, Japan*

https://doi.org/10.1021/acsenergylett.4c03233
ACS Energy Lett. 2025, 10, 915−924

Kaihuai Du − *Institute of Technology for Carbon Neutralization, Yangzhou University, Yangzhou 225127 Jiangsu, China*
Chengyang Liu − *Institute for Energy Research, School of Energy and Power Engineering, School of Environment and Safety Engineering, Jiangsu University, Zhenjiang 212013, China*
Cheng Chen − *Institute for Energy Research, School of Energy and Power Engineering, School of Environment and Safety Engineering, Jiangsu University, Zhenjiang 212013, China;* orcid.org/0000-0003-0770-795X
Haoxin Wang − *Institute for Energy Research, School of Energy and Power Engineering, School of Environment and Safety Engineering, Jiangsu University, Zhenjiang 212013, China;* orcid.org/0000-0001-7421-4245
Ziyang Xia − *Institute for Energy Research, School of Energy and Power Engineering, School of Environment and Safety Engineering, Jiangsu University, Zhenjiang 212013, China*
Jinman Yang − *Institute for Energy Research, School of Energy and Power Engineering, School of Environment and Safety Engineering, Jiangsu University, Zhenjiang 212013, China*
Hui Xu − *Institute for Energy Research, School of Energy and Power Engineering, School of Environment and Safety Engineering, Jiangsu University, Zhenjiang 212013, China*
Toshinori Matsushima − *International Institute for Carbon-Neutral Energy Research (WPI-I2CNER), Kyushu University, Fukuoka 819-0395, Japan*
Zhanglin Guo − *International Institute for Carbon-Neutral Energy Research (WPI-I2CNER), Kyushu University, Fukuoka 819-0395, Japan;* orcid.org/0000-0003-3168-2588
Meng Li − *Key Lab for Special Functional Materials of Ministry of Education, National & Local Joint Engineering Research Center for High-efficiency Display and Lighting Technology, School of Materials Science and Engineering, Collaborative Innovation Center of Nano Functional Materials and Applications, Henan University, Kaifeng 475004, P. R. China*
Antonio Abate − *Helmholtz-Zentrum Berlin für Materialien und Energie GmbH, Berlin 14109, Germany;* orcid.org/0000-0002-3012-3541
Paul J. Dyson − *Institute of Chemical Sciences and Engineering, École Polytechnique Fédérale de Lausanne (EPFL), CH-1015 Lausanne, Switzerland;* orcid.org/0000-0003-3117-3249
Mohammad Khaja Nazeeruddin − *Institute of Chemical Sciences and Engineering, École Polytechnique Fédérale de Lausanne (EPFL), CH-1015 Lausanne, Switzerland;* orcid.org/0000-0001-5955-4786

Complete contact information is available at: https://pubs.acs.org/10.1021/acsenergylett.4c03233

Author Contributions

[▽]M. Z., K. D.: These authors contributed equally to this work.

Author Contributions

M. Z. and K. D. contributed equally to this work. M. C. supervised the project. M. C., M. Z., A. W., and G. L. conceived the idea and designed the experiments. M. Z. and C. L. synthesized and characterized the hole transport materials. M. Z. and K. D. fabricated small devices and modules. J. Y. and H. X. performed the DFT calculations. C. C., H. W., and M. L. provided testing support and interpreted the data. Z. X. analyzed the carrier dynamics. T. M. and Z. G. helped with PESA and energetic ordering tests. A. A., P. J. D., and M. K. N. provided much help with the results and discussion, test instructions, and paper writing. M. Z., A. W., and G. L. wrote the manuscript with input from all other authors.

Notes

The authors declare no competing financial interest.

■ ACKNOWLEDGMENTS

This work was supported by the National Natural Science Foundation of China (Grants 22179053, 22279046), Natural Science Excellent Youth Foundation of Jiangsu Provincial (BK20220112), Special Foundation for Carbon Peak Carbon Neutralization Technology Innovation Program of Jiangsu Province (BE2022026-2), Helmholtz-Zentrum Berlin (HZB), and École Polytechnique Fédérale de Lausanne (EPFL). The authors thank Shiyanjia Lab (www.shiyanjia.com) for assistance with the NMR spectroscopy, TGA measurements from SCI-GO (www.sci-go.com), and UPS measurements from Beijing Zhongkebaice Technology Service Co., Ltd. (www.zkbaice.cn).

■ REFERENCES

(1) Min, H.; Lee, D. Y.; Kim, J.; Kim, G.; Lee, K. S.; Kim, J.; Paik, M. J.; Kim, Y. K.; Kim, K. S.; Kim, M. G.; et al. Perovskite solar cells with atomically coherent interlayers on SnO2 electrodes. *Nature* **2021**, *598* (7881), 444−450.
(2) Fei, C.; Li, N.; Wang, M.; Wang, X.; Gu, H.; Chen, B.; Zhang, Z.; Ni, Z.; Jiao, H.; Xu, W.; et al. Lead-chelating hole-transport layers for efficient and stable perovskite minimodules. *Science* **2023**, *380* (6647), 823−829.
(3) Chen, H.; Liu, C.; Xu, J.; Maxwell, A.; Zhou, W.; Yang, Y.; Zhou, Q.; Bati, A. S. R.; Wan, H.; Wang, Z.; et al. Improved charge extraction in inverted perovskite solar cells with dual-site-binding ligands. *Science* **2024**, *384* (6692), 189−193.
(4) Zhou, J.; Tan, L.; Liu, Y.; Li, H.; Liu, X.; Li, M.; Wang, S.; Zhang, Y.; Jiang, C.; Hua, R.; et al. Highly efficient and stable perovskite solar cells via a multifunctional hole transporting material. *Joule* **2024**, *8* (6), 1691−1706.
(5) Qu, G.; Cai, S.; Qiao, Y.; Wang, D.; Gong, S.; Khan, D.; Wang, Y.; Jiang, K.; Chen, Q.; Zhang, L.; et al. Conjugated linker-boosted self-assembled monolayer molecule for inverted perovskite solar cells. *Joule* **2024**, *8*, 2123−2134.
(6) Park, J.; Kim, J.; Yun, H. S.; Paik, M. J.; Noh, E.; Mun, H. J.; Kim, M. G.; Shin, T. J.; Seok, S. I. Controlled growth of perovskite layers with volatile alkylammonium chlorides. *Nature* **2023**, *616* (7958), 724−730.
(7) Park, N.-G.; Grätzel, M.; Miyasaka, T.; Zhu, K.; Emery, K. Towards stable and commercially available perovskite solar cells. *Nat. Energy* **2016**, *1* (11), 16152.
(8) Heo, J. H.; Im, S. H.; Noh, J. H.; Mandal, T. N.; Lim, C.-S.; Chang, J. A.; Lee, Y. H.; Kim, H.-j.; Sarkar, A.; Nazeeruddin, M. K.; et al. Efficient inorganic−organic hybrid heterojunction solar cells containing perovskite compound and polymeric hole conductors. *Nat. Photonics* **2013**, *7* (6), 486−491.
(9) Jung, E. H.; Jeon, N. J.; Park, E. Y.; Moon, C. S.; Shin, T. J.; Yang, T.-Y.; Noh, J. H.; Seo, J. Efficient, stable and scalable perovskite solar cells using poly(3-hexylthiophene). *Nature* **2019**, *567* (7749), 511−515.
(10) Zhang, C.; Wei, K.; Hu, J.; Cai, X.; Du, G.; Deng, J.; Luo, Z.; Zhang, X.; Wang, Y.; Yang, L.; Zhang, J. A review on organic hole transport materials for perovskite solar cells: Structure, composition and reliability. *Mater. Today* **2023**, *67*, 518−547.
(11) Zhang, S.; Ye, F.; Wang, X.; Chen, R.; Zhang, H.; Zhan, L.; Jiang, X.; Li, Y.; Ji, X.; Liu, S.; et al. Minimizing buried interfacial

defects for efficient inverted perovskite solar cells. *Science* **2023**, *380* (6643), 404−409.
(12) Fu, Q.; Tang, X.; Liu, H.; Wang, R.; Liu, T.; Wu, Z.; Woo, H. Y.; Zhou, T.; Wan, X.; Chen, Y.; Liu, Y. Ionic Dopant-Free Polymer Alloy Hole Transport Materials for High-Performance Perovskite Solar Cells. *J. Am. Chem. Soc.* **2022**, *144* (21), 9500−9509.
(13) Zhang, T.; Wang, F.; Kim, H.-B.; Choi, I.-W.; Wang, C.; Cho, E.; Konefal, R.; Puttisong, Y.; Terado, K.; Kobera, L.; et al. Ion-modulated radical doping of spiro-OMeTAD for more efficient and stable perovskite solar cells. *Science* **2022**, *377* (6605), 495−501.
(14) Lee, M. M.; Teuscher, J.; Miyasaka, T.; Murakami, T. N.; Snaith, H. J. Efficient hybrid solar cells based on meso-superstructured organometal halide perovskites. *Science* **2012**, *338* (6107), 643−647.
(15) Zhai, M. D.; Li, M.; Deng, Z. J.; Yao, R. G.; Wang, L. Q.; Chen, C.; Wang, H. X.; Ding, X. D.; Liu, L. C.; Li, X.; Cheng, M. Perovskite Solar Cells and Modules Employing Facile Synthesis and Green-Solvent-Processable Organic Hole Transport Materials. *ACS Energy Lett.* **2023**, *8* (11), 4966−4975.
(16) Gao, K.; Xu, B.; Hong, C.; Shi, X.; Liu, H.; Li, X.; Xie, L.; Jen, A. K. Y. Di-Spiro-Based Hole-Transporting Materials for Highly Efficient Perovskite Solar Cells. *Adv. Energy Mater.* **2018**, *8* (22), 1800809.
(17) Burschka, J.; Kessler, F.; Nazeeruddin, M. K.; Grätzel, M. Co(III) Complexes as p-Dopants in Solid-State Dye-Sensitized Solar Cells. *Chem. Mater.* **2013**, *25* (15), 2986−2990.
(18) Wang, S.; Sina, M.; Parikh, P.; Uekert, T.; Shahbazian, B.; Devaraj, A.; Meng, Y. S. Role of 4-tert-Butylpyridine as a Hole Transport Layer Morphological Controller in Perovskite Solar Cells. *Nano Lett.* **2016**, *16* (9), 5594−5600.
(19) Yang, H.; Xu, T.; Chen, W.; Wu, Y.; Guo, X.; Shen, Y.; Ding, C.; Chen, X.; Chen, H.; Ding, J.; et al. Iodonium Initiators: Paving the Air-free Oxidation of Spiro-OMeTAD for Efficient and Stable Perovskite Solar Cells. *Angew. Chem., Int. Ed.* **2024**, *63* (5), No. e202316183.
(20) Ren, Y.; Ren, M.; Xie, X.; Wang, J.; Cai, Y.; Yuan, Y.; Zhang, J.; Wang, P. A spiro-OMeTAD based semiconductor composite with over 100 °C glass transition temperature for durable perovskite solar cells. *Nano Energy* **2021**, *81*, 105655.
(21) Zhang, X.; Liu, X.; Tirani, F. F.; Ding, B.; Chen, J.; Rahim, G.; Han, M.; Zhang, K.; Zhou, Y.; Quan, H.; et al. Dopant-Free Pyrene-Based Hole Transporting Material Enables Efficient and Stable Perovskite Solar Cells. *Angew. Chem., Int. Ed.* **2024**, *63* (18), No. e202320152.
(22) Liu, X.; Wang, K.; Li, Y.; You, S.; Liu, T.; Lv, Y.; Li, Y.; Wang, Y.; He, H.; Li, Y.; et al. Mesoscale Ordering 3D Mosaic Self-Assembly of Dopant-Free Hole Transport Material for Perovskite Solar Cells. *ACS Energy Lett.* **2024**, *9* (5), 2446−2455.
(23) Xie, G.; Wang, J.; Yin, S.; Liang, A.; Wang, W.; Chen, Z.; Feng, C.; Yu, J.; Liao, X.; Fu, Y.; et al. Dual-Strategy Tailoring Molecular Structures of Dopant-Free Hole Transport Materials for Efficient and Stable Perovskite Solar Cells. *Angew. Chem., Int. Ed.* **2024**, *63* (20), No. e202403083.
(24) Ji, X.; Zhou, T.; Fu, Q.; Wang, W.; Wu, Z.; Zhang, M.; Guo, X.; Liu, D.; Woo, H. Y.; Liu, Y. Dopant-Free Two-Dimensional Hole Transport Small Molecules Enable Efficient Perovskite Solar Cells. *Adv. Energy Mater.* **2023**, *13* (11), 2203756.
(25) Xie, Z.; Park, H.; Choi, S.; Park, H. Y.; Gokulnath, T.; Kim, H.; Kim, J.; Kim, H. B.; Choi, I. W.; Jo, Y.; et al. Thienothiophene-Assisted Property Optimization for Dopant-Free π-Conjugation Polymeric Hole Transport Material Achieving Over 23% Efficiency in Perovskite Solar Cells. *Adv. Energy Mater.* **2023**, *13* (2), 2202680.
(26) Zhang, H.; Yu, X.; Li, M.; Zhang, Z.; Song, Z.; Zong, X.; Duan, G.; Zhang, W.; Chen, C.; Zhang, W.-H.; et al. Benzothieno[3,2-b]thiophene-Based Noncovalent Conformational Lock Achieves Perovskite Solar Cells with Efficiency over 24%. *Angew. Chem., Int. Ed.* **2023**, *62* (52), No. e202314270.
(27) Jeong, M.; Choi, I. W.; Yim, K.; Jeong, S.; Kim, M.; Choi, S. J.; Cho, Y.; An, J. H.; Kim, H. B.; Jo, Y.; et al. Large-area perovskite solar cells employing spiro-Naph hole transport material. *Nat. Photonics* **2022**, *16* (2), 119−125.
(28) Liu, X.; Ding, B.; Han, M.; Yang, Z.; Chen, J.; Shi, P.; Xue, X.; Ghadari, R.; Zhang, X.; Wang, R.; et al. Extending the pi-Conjugated System in Spiro-Type Hole Transport Material Enhances the Efficiency and Stability of Perovskite Solar Modules. *Angew. Chem., Int. Ed.* **2023**, *62* (29), No. e202304350.
(29) Han, M.; Liang, Y.; Chen, J.; Zhang, X.; Ghadari, R.; Liu, X.; Wu, N.; Wang, Y.; Zhou, Y.; Ding, Y.; et al. A N-Ethylcarbazole-Terminated Spiro-Type Hole-Transporting Material for Efficient and Stable Perovskite Solar Cells. *ChemSusChem* **2022**, *15* (20), No. e202201485.
(30) Ren, Y.; Wei, Y.; Li, T.; Mu, Y.; Zhang, M.; Yuan, Y.; Zhang, J.; Wang, P. Spirobifluorene with an asymmetric fluorenylcarbazolamine electron-donor as the hole transport material increases thermostability and efficiency of perovskite solar cells. *Energy Environ. Sci.* **2023**, *16* (8), 3534−3542.
(31) Jeon, N. J.; Na, H.; Jung, E. H.; Yang, T.-Y.; Lee, Y. G.; Kim, G.; Shin, H.-W.; Il Seok, S.; Lee, J.; Seo, J. A fluorene-terminated hole-transporting material for highly efficient and stable perovskite solar cells. *Nat. Energy* **2018**, *3* (8), 682−689.
(32) Zhai, M.; Miao, Y.; Chen, C.; Liu, L.; Wang, H.; Ding, X.; Xia, Z.; Wang, L.; Cheng, M. Modulating donor assemblies of D-π-D type hole transport materials for perovskite solar cells. *J. Power Sources* **2022**, *551*, 232199.
(33) Christians, J. A.; Schulz, P.; Tinkham, J. S.; Schloemer, T. H.; Harvey, S. P.; Tremolet de Villers, B. J.; Sellinger, A.; Berry, J. J.; Luther, J. M. Tailored interfaces of unencapsulated perovskite solar cells for > 1,000 h operational stability. *Nat. Energy* **2018**, *3* (1), 68−74.
(34) Fu, Q.; Liu, H.; Gao, Y.; Cao, X.; Li, Y.; Yang, Y.; Wang, J.; Chen, Y.; Yao, Z.; Liu, Y. Tunable Molecular Packing of Dopant-Free Hole-Transport Polymers for Perovskite Solar Cells. *ACS Energy Lett.* **2023**, *8* (7), 2878−2885.
(35) Wu, B.; Fu, Q.; Sun, L.; Liu, Y.; Sun, Z.; Xue, S.; Liu, Y.; Liang, M. Conjugation Engineering of Spiro-Based Hole Transport Materials for Efficient and Stable Perovskite Solar Cells. *ACS Energy Lett.* **2022**, *7* (8), 2667−2676.
(36) Abbaszadeh, D.; Kunz, A.; Wetzelaer, G. A. H.; Michels, J. J.; Crăciun, N. I.; Koynov, K.; Lieberwirth, I.; Blom, P. W. M. Elimination of charge carrier trapping in diluted semiconductors. *Nat. Mater.* **2016**, *15* (6), 628−633.
(37) Shao, Y.; Yuan, Y.; Huang, J. Correlation of energy disorder and open-circuit voltage in hybrid perovskite solar cells. *Nat. Energy* **2016**, *1* (1), 15001.
(38) Cheng, Q.; Chen, H.; Yang, F.; Chen, Z.; Chen, W.; Yang, H.; Shen, Y.; Ou, X. M.; Wu, Y.; Li, Y.; Li, Y. Molecular Self-Assembly Regulated Dopant-Free Hole Transport Materials for Efficient and Stable n-i-p Perovskite Solar Cells and Scalable Modules. *Angew. Chem., Int. Ed. Engl.* **2022**, *61* (42), No. e202210613.
(39) Zhang, C.; Liao, Q.; Chen, J.; Li, B.; Xu, C.; Wei, K.; Du, G.; Wang, Y.; Liu, D.; Deng, J.; et al. Thermally Crosslinked Hole Conductor Enables Stable Inverted Perovskite Solar Cells with 23.9% Efficiency. *Adv. Mater.* **2023**, *35* (9), No. e2209422.
(40) Rakstys, K.; Abate, A.; Dar, M. I.; Gao, P.; Jankauskas, V.; Jacopin, G.; Kamarauskas, E.; Kazim, S.; Ahmad, S.; Gratzel, M.; Nazeeruddin, M. K. Triazatruxene-Based Hole Transporting Materials for Highly Efficient Perovskite Solar Cells. *J. Am. Chem. Soc.* **2015**, *137* (51), 16172−16178.
(41) Luo, Y.; Chitumalla, R. K.; Ham, S.-Y.; Cakan, D. N.; Kim, T.; Paek, S.; Meng, Y. S.; Jang, J.; Fenning, D. P.; Kim, M.-c. A Si-Substituted Spirobifluorene Hole-Transporting Material for Perovskite Solar Cells. *ACS Energy Lett.* **2023**, *8* (12), 5003−5011.
(42) Zhang, Z.; Yuan, L.; Li, B.; Luo, H.; Wang, S.; Li, Z.; Xing, Y.; Wang, J.; Dong, P.; Guo, K.; et al. A Trifluoroethoxyl Functionalized Spiro-Based Hole-Transporting Material for Highly Efficient and Stable Perovskite Solar Cells. *Sol. RRL* **2022**, *6* (2), 2100944.
(43) Mabrouk, S.; Zhang, M.; Wang, Z.; Liang, M.; Bahrami, B.; Wu, Y.; Wu, J.; Qiao, Q.; Yang, S. Dithieno[3,2-b:2′,3′-d]pyrrole-based

hole transport materials for perovskite solar cells with efficiencies over 18%. *J. Mater. Chem. A* **2018**, *6* (17), 7950−7958.
(44) Schwenzer, J. A.; Hellmann, T.; Nejand, B. A.; Hu, H.; Abzieher, T.; Schackmar, F.; Hossain, I. M.; Fassl, P.; Mayer, T.; Jaegermann, W.; et al. Thermal Stability and Cation Composition of Hybrid Organic−Inorganic Perovskites. *ACS Appl. Mater. Interfaces* **2021**, *13* (13), 15292−15304.
(45) Zhai, M.; Ma, L.; Cai, C.; Xia, Z.; Peng, D.; Wang, L.; Chen, C.; Wu, T.; Hua, Y.; Wang, H.; et al. Construction of Efficient Cs2AgBiBr6 Perovskite Solar Cells by Enhancing Hole-Selective Contact with Deep-Level Dopant-Free Hole Transport Material. *Adv. Funct. Mater.* **2024**, *34* (27), 2315428.
(46) Li, D.; Huang, Y.; Ma, R.; Liu, H.; Liang, Q.; Han, Y.; Ren, Z.; Liu, K.; Fong, P. W.-K.; Zhang, Z.; et al. Surface Regulation with Polymerized Small Molecular Acceptor Towards Efficient Inverted Perovskite Solar Cells. *Adv. Energy Mater.* **2023**, *13* (18), 2204247.
(47) Lan, Z.; Huang, H.; Du, S.; Lu, Y.; Sun, C.; Yang, Y.; Zhang, Q.; Suo, Y.; Qu, S.; Wang, M.; et al. Cascade Reaction in Organic Hole Transport Layer Enables Efficient Perovskite Solar Cells. *Angew. Chem., Int. Ed.* **2024**, *63* (21), No. e202402840.
(48) Zhou, J.; Li, H.; Tan, L.; Liu, Y.; Yang, J.; Hua, R.; Yi, C. Tuning Hole Transport Properties via Pyrrole Derivation for High-Performance Perovskite Solar Cells. *Angew. Chem., Int. Ed.* **2023**, *62* (15), No. e202300314.
(49) Jiang, W.; Li, F.; Li, M.; Qi, F.; Lin, F. R.; Jen, A. K. Y. π-Expanded Carbazoles as Hole-Selective Self-Assembled Monolayers for High-Performance Perovskite Solar Cells. *Angew. Chem., Int. Ed.* **2022**, *61* (51), No. e202213560.
(50) Ponseca, C. S., Jr.; Chábera, P.; Uhlig, J.; Persson, P.; Sundström, V. Ultrafast Electron Dynamics in Solar Energy Conversion. *Chem. Rev.* **2017**, *117* (16), 10940−11024.
(51) Zhao, W.; Wu, M.; Liu, Z.; Yang, S.; Li, Y.; Wang, J.; Yang, L.; Han, Y.; Liu, S. Orientation Engineering via 2D Seeding for Stable 24.83% Efficiency Perovskite Solar Cells. *Adv. Energy Mater.* **2023**, *13* (14), 2204260.
(52) Wang, S.; Khan, D.; Zhou, W.; Sui, Y.; Zhang, T.; Yu, G.; Huang, Y.; Yang, X.; Chen, X.; Yan, H.; et al. Ion-Dipole Interaction for Self-Assembled Monolayers: A New Strategy for Buried Interface in Inverted Perovskite Solar Cells. *Adv. Funct. Mater.* **2024**, *34* (27), 2316202.
(53) Rajagopal, A.; Liang, P.-W.; Chueh, C.-C.; Yang, Z.; Jen, A. K. Y. Defect Passivation via a Graded Fullerene Heterojunction in Low-Bandgap Pb−Sn Binary Perovskite Photovoltaics. *ACS Energy Lett.* **2017**, *2* (11), 2531−2539.

https://doi.org/10.1021/acsenergylett.4c03233
ACS Energy Lett. 2025, 10, 915−924